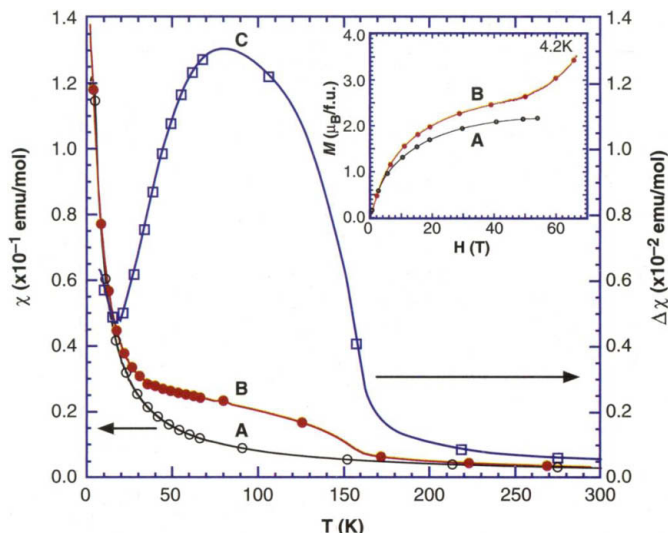


Fig. 5. Temperature dependence of the susceptibility of (A) CPL-1 and (B) CPL-1 with O₂ molecules, and (C) the differences between (A) and (B), correspond to the contribution from adsorbed O₂ molecules. (Inset) High-field magnetization process of (A) CPL-1 and (B) with O₂ molecules. χ , susceptibility; M , magnetization; μ_B , bohr magneton; f.u., formula unit; H , magnet-ic field T , temperature.



(2I), comparable with that of α phase at a pressure of 2 GPa.

The confinement effect and the restricted geometry resulting from 1D nanochannels of CPL-1 lead to a specific molecular assembly: a 1D ladder structure constructed of O₂ dimers, which is unlikely to be bulk fluid and/or solid.

References and Notes

1. W. Mori *et al.*, *Mol. Cryst. Liq. Cryst.* **306**, 1 (1997).
2. U. Köbler, R. Marx, *Phys. Rev. B* **35**, 9809 (1987).
3. H. Kanoh, A. Zamma, N. Setoyama, Y. Hanzawa, K. Kaneko, *Langmuir* **13**, 1047 (1997).
4. W. A. Steele, *Langmuir* **12**, 145 (1996).
5. M. Eddaoudi *et al.*, *Acc. Chem. Res.* **34**, 319 (2001).

6. B. Moulton, M. J. Zaworotko, *Chem. Rev.* **101**, 1629 (2001).
7. S. Noro, S. Kitagawa, M. Kondo, K. Seki, *Angew. Chem. Int. Ed. Engl.* **39**, 2082 (2000).
8. K. Seki, *Chem. Commun.* **16**, 1496 (2001).
9. M. Takata, E. Nishibori, M. Sakata, *Z. Kristallogr.* **216**, 71 (2001).
10. M. Takata *et al.*, *Nature* **377**, 46 (1995).
11. C.-R. Wang *et al.*, *Nature* **408**, 426 (2000).
12. E. Nishibori *et al.*, *J. Phys. Chem. Solids* **62**, 2095 (2001).
13. M. Kondo *et al.*, *Angew. Chem. Int. Ed. Engl.* **38**, 140 (1999).
14. R. Kitaura, K. Fujimoto, S. Noro, M. Kondo, S. Kitagawa, *Angew. Chem. Int. Ed. Engl.* **41**, 133 (2002).
15. The space group was assigned as $P2_1/c$, and the lattice parameters were determined by Rietveld analysis as follows, $a = 4.71534(6)$ Å, $b = 19.8280(2)$ Å, $c = 10.7184(1)$ Å, and $\beta = 95.1031(10)^\circ$. R_{wp} and R_i were 2.6 and 3.3%, respectively.
16. The MEM analysis was carried out by the computer

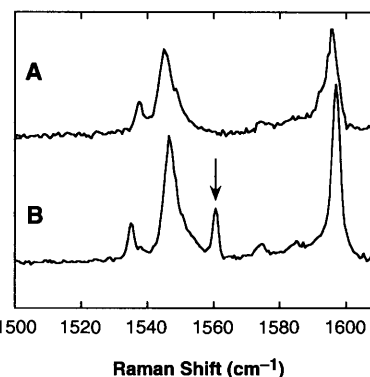


Fig. 6. Raman spectra of (A) CPL-1 and (B) CPL-1 with O₂ molecules. A peak due to the stretching of O₂ molecules (marked by an arrow) is shown in (B). The abscissas were calibrated using the standard lines from a neon lamp, and the resolution of the data is 0.6 cm⁻¹.

- program ENIGMA. The unit cell was divided into pixels (128 by 512 by 256) in calculation.
17. H. Tanaka *et al.*, *J. Appl. Crystallogr.* **35**, 282 (2002).
18. M. Miyahara, K. E. Gubbins, *J. Chem. Phys.* **106**, 2865 (1997).
19. J. O. Hirschfelder, C. F. Curtiss, R. B. Bird, *Molecular Theory of Gases and Liquids* (Wiley, New York, 1954).
20. C. Ueda, K. Sugiyama, M. Date, *J. Phys. Soc. Jpn.* **54**, 1107 (1985).
21. K. Bier, H. Jodl, *J. Chem. Phys.* **81**, 1192 (1984).
22. The synchrotron radiation experiments were performed at the Spring-8 with the approval of the Japan Synchrotron Radiation Research Institute (JASRI). We thank H. Tanaka for the computer program ENIGMA for the MEM analysis, K. Kato for his experimental help at Spring-8, and K. Miura for providing adsorption measurement apparatus. Supported by a grant-in-aid for Scientific Research from the Ministry of Education, Culture, Science, Sports and Technology of Japan.

16 September 2002; accepted 13 November 2002

Structure-Assigned Optical Spectra of Single-Walled Carbon Nanotubes

Sergei M. Bachilo,¹ Michael S. Strano,¹ Carter Kittrell,¹ Robert H. Hauge,¹ Richard E. Smalley,^{1,2} R. Bruce Weisman^{1*}

Spectrofluorimetric measurements on single-walled carbon nanotubes (SWNTs) isolated in aqueous surfactant suspensions have revealed distinct electronic absorption and emission transitions for more than 30 different semiconducting nanotube species. By combining these fluorimetric results with resonance Raman data, each optical transition has been mapped to a specific (n,m) nanotube structure. Optical spectroscopy can thereby be used to rapidly determine the detailed composition of bulk SWNT samples, providing distributions in both tube diameter and chiral angle. The measured transition frequencies differ substantially from simple theoretical predictions. These deviations may reflect combinations of trigonal warping and excitonic effects.

Many of the major challenges currently facing basic and applied research on SWNTs arise from the diversity of tube diameters and chiral angles in samples formed through any preparative method. Because the electronic

and optical properties of nanotubes vary substantially with structure (1), these samples show mixed characteristics that hinder basic investigations and limit some of the most promising applications. The recent discovery

of band-gap fluorescence from semiconducting SWNTs in aqueous micelle-like suspensions (2) opens the door to powerful experimental approaches that can extract the spectroscopic properties of specific tube structures through bulk measurements. We report such a spectrofluorimetric study, in which distinct first and second van Hove optical transitions are measured for 33 different nanotube species and then assigned to specific structures. Our findings provide a tool for analyzing the detailed composition of bulk nanotube samples, one that can be adapted to monitor and guide processes aimed at separating tubes by type.

Figure 1A illustrates how each SWNT structure is indexed by two integers (n,m) that

¹Department of Chemistry, Center for Nanoscale Science and Technology, and Center for Biological and Environmental Nanotechnology, Rice University, 6100 Main Street, Houston, TX 77005, USA. ²Department of Physics, Rice University, 6100 Main Street, Houston, TX 77005, USA.

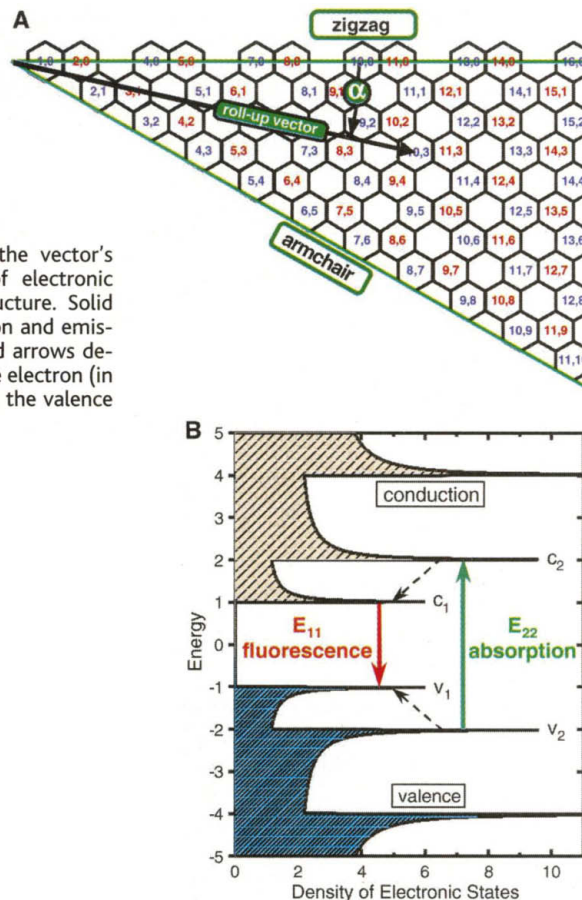
*To whom correspondence should be addressed. E-mail: weisman@rice.edu

define the length (π times the tube diameter, d_t) and chiral angle (α) of that tube's roll-up vector on a graphene sheet. We omit structures having $n - m$ evenly divisible by 3, because they are metals or semimetals and will not fluoresce. Figure 1B shows the qualitative pattern of sharp van Hove peaks, which arise from quasi-one-dimensionality, predicted for electronic state densities of semiconducting SWNTs. As shown in the figure, light absorption at photon energy E_{22} is followed by fluorescence emission near E_{11} . The values of E_{11} and E_{22} will vary with tube structure (3). To study these transitions, we first processed SWNTs grown in high-pressure carbon monoxide (HiPco) to obtain samples rich in individual nanotubes suspended by SDS surfactant in deuterium oxide (2). We then performed spectroscopic measurements using a commercial spectrofluorometer (a J-Y Spex Fluorolog 3-211) equipped with an indium-gallium-arsenide near-infrared detector cooled by liquid nitrogen. Emission intensity was measured as a function of both excitation wavelength (from 300 to 930 nm) and emission wavelength (from 810 to 1550 nm), with 3-nm steps and 7-nm spectral slit widths on both axes. The resulting 52,000 measurements were corrected for instrumental variations in excitation intensity and detection sensitivity to give the results shown in Fig. 2A as a contour plot.

The white oval drawn in Fig. 2A marks a region of special interest that contains discrete peaks, arising from the transitions shown in Fig. 1B, in various semiconducting nanotube species. Careful analysis reveals 33 such features. All absorption peaks in this region are also peaks for fluorescence excitation. Additional peaks at shorter excitation wavelengths are attributed to $v_3 \rightarrow c_3$ excitation followed by $c_1 \rightarrow v_1$ emission in the same set of nanotubes (Fig. 1B). Between these two branches of peaks lies a region that shows very low emission intensity despite strong absorption. We attribute this non-emissive region to metallic and semimetallic nanotubes in the sample, which are expected to absorb between the semiconductors' $v_2 \rightarrow c_2$ and $v_3 \rightarrow c_3$ branches (4) but not to emit measurable luminescence. Several of the features outside the circled region at longer excitation wavelengths are $v_1 \rightarrow c_1$ vibronic bands (electronic transitions with vibrational excitation). Within the circled region of current interest, many spectral features that overlap in simple emission or absorption spectra are clearly separated in our two-dimensional excitation-emission spectrum. The coordinates of each peak in this region give the $v_2 \rightarrow c_2$ optical excitation energy ($E_{22} = hc/\lambda_{22} = hc\bar{\nu}_{22}$) and the corresponding $c_1 \rightarrow v_1$ emission energy ($E_{11} = hc/\lambda_{11} = hc\bar{\nu}_{11}$) for one semiconducting nanotube species (h is Planck's constant, c is the speed of light, λ is photon wavelength, and $\bar{\nu}$ is photon frequency in cm^{-1}).

A crucial goal is to identify the specific

Fig. 1. Physical and electronic structures of semiconducting SWNTs. (A) Graphene sheet segment showing indexed lattice points. Nanotubes designated (n,m) are obtained by rolling the sheet from $(0,0)$ to (n,m) along a roll-up vector. The chiral angle α (from 0 to 30°) is measured between that vector and the zigzag axis; the tube circumference is the vector's length. (B) Schematic density of electronic states for a single nanotube structure. Solid arrows depict the optical excitation and emission transitions of interest; dashed arrows denote nonradiative relaxation of the electron (in the conduction band) and hole (in the valence band) before emission.



(n,m) nanotube structure that gives each observed spectral peak. The circles in Fig. 2B plot experimental spectral peak positions in the region of interest. Clear patterns are evident, as shown by the solid curves drawn through the data points. To help interpret these patterns, we plotted the ratio of optical excitation to emission energies for each peak versus the peak's excitation wavelength. The result is shown in Fig. 2C. The pattern of solid lines through these experimental points qualitatively resembles the pattern shown in Fig. 2D, which displays computed findings from an extended tight-binding model calculation on SWNTs (5). In this computation, lines have been drawn through points of species that share the same value of $n - m$. We refer to these sets as nanotube families. The analogy between the simulation of Fig. 2D and the experimental pattern of Fig. 2C lets us sort the observed data points into families marked by the solid lines in Fig. 2C (or the black lines in Fig. 2B). Another step in the assignment process is recognizing that, within a family, the values of n and m for any point must both be one greater than for the adjacent point at a shorter wavelength. Also, the simulation shows that the transition energy ratios deviate increasingly from a central value as the value of $n - m$ increases. The direction of this deviation depends on whether dividing $n - m$ by 3 leaves a remainder (mod) of 1 or 2 (6, 7). (We refer to

these two subsets as "mod 3 = 1" and "mod 3 = 2" structures, respectively; "mod 3 = 0" tubes are absent from our fluorescence data because they are metallic or semimetallic.) This pattern of family ratios provides a third step in deducing the assignment. A further important step is the linkage pattern across families illustrated by the colored curves in Fig. 2B (a subset of which are drawn as dashed curves in Fig. 2C). Simulation shows that adjacent points on these curves differ either by +1 in n value and -2 in m value, or by +2 in n and -1 in m (8).

The relations outlined above combine to define a complete connectivity that maps the whole pattern of experimental spectral features onto the array of nanotube structures symbolized by points on a graphene lattice (Fig. 1A). However, the assignment mapping remains ambiguous until it is "anchored" by determining the specific (n,m) values associated with a particular spectral transition. We found that there are a few plausible global assignments defined by closely related anchor choices. To select from among these, we measured resonance Raman spectra on our samples using several laser wavelengths. It is well known that the radial breathing mode (RBM) frequency of SWNTs has a simple monotonic relation to tube diameter, and that Raman scattering from this mode is strongly and selectively enhanced when the photon

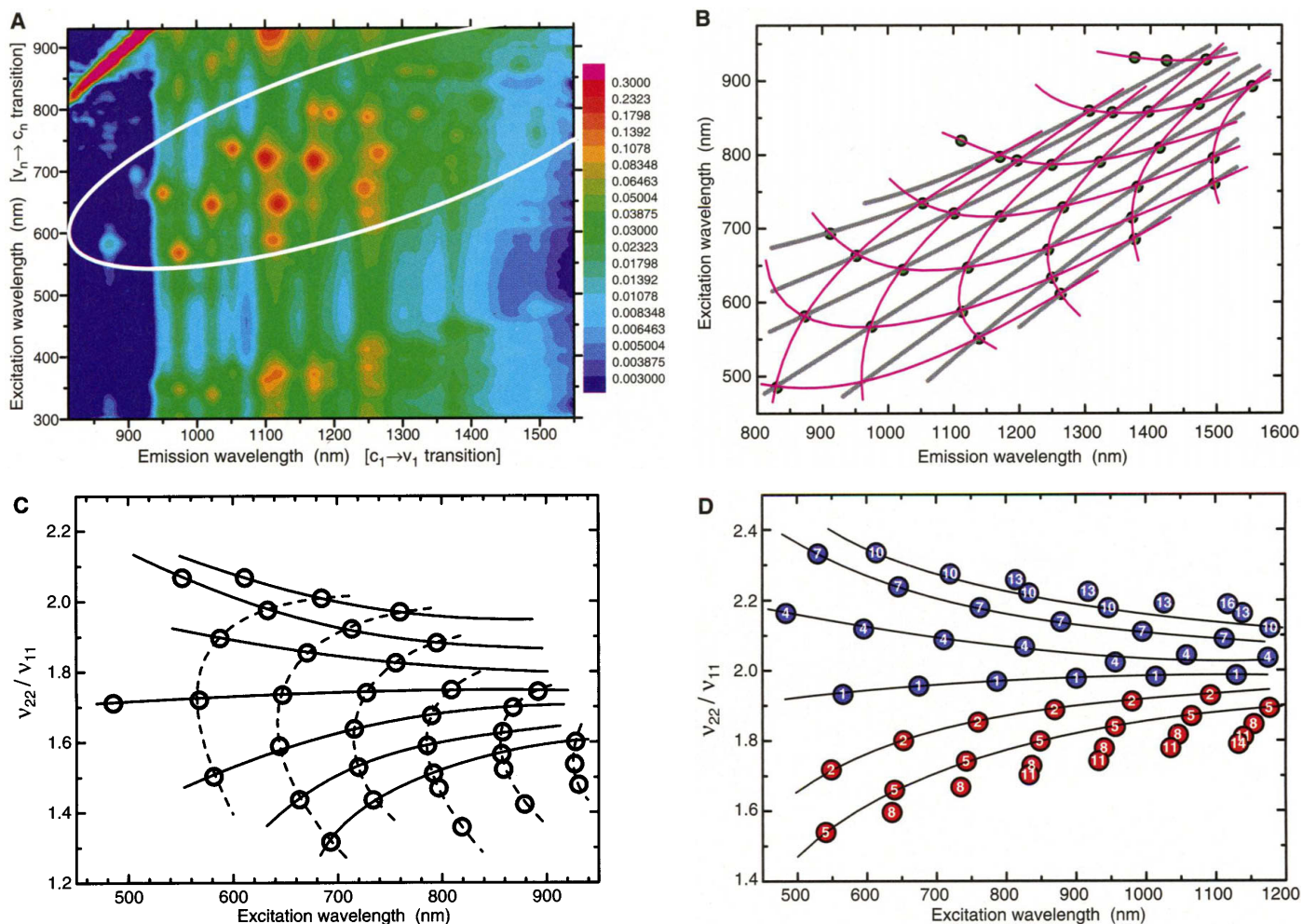


Fig. 2. (A) Contour plot of fluorescence intensity versus excitation and emission wavelengths for a sample of SWNTs suspended in SDS and deuterium oxide. The white oval encloses transitions plotted in (B) and (C). (B) Circles show spectral peak positions from (A); lines show perceived patterns in the data. (C) Measured ratios of excitation to emission frequencies for excitation to emission frequencies shown in (B), plotted versus exci-

tation wavelength. Solid and dashed lines show perceived patterns. (D) Computed E_{22}/E_{11} energy ratios plotted versus excitation wavelength (λ_{11}) for an extended tight binding model of nanotube electronic structure. Blue symbols indicate $(n - m) \bmod 3 = 1$; red symbols indicate $(n - m) \bmod 3 = 2$. Numbers in symbols give the value of $n - m$, and lines connect families with equal $n - m$ values.

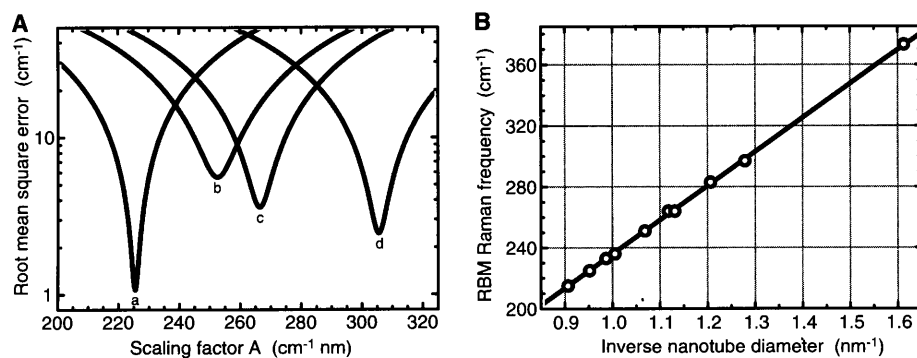


Fig. 3. (A) Plots of rms error in fitting a set of 10 observed Raman RBM frequencies (listed in 1), using the two-parameter fitting function given in the text, as a function of parameter A with parameter B optimized. Each curve arises from a different possible assignment of optical transitions to nanotube structures. Optimized values of B (in cm^{-1}) are 12.5 for curve “a,” 5.0 for “b,” -16.0 for “c,” and -34.4 for “d.” The feature with $\lambda_{11} = 873$ nm is assigned to (6,4) in “a,” the chosen assignment; (8,3) in “b”; (6,5) in “c”; and (7,5) in “d.” (B) Observed RBM frequencies as a function of deduced inverse nanotube diameter for the chosen assignment, “a.” The solid line is computed using parameters $A = 223.5 \text{ cm}^{-1} \text{ nm}$ and $B = 12.5 \text{ cm}^{-1}$.

energy matches a nanotube’s optical transition (9–12). From our Raman measurements, we compiled a set of 10 RBM frequencies

that were correlated with specific spectral features of the data in Fig. 2A. A candidate assignment was tentatively invoked to give

(n, m) values, and thereby tube diameters, for each spectral feature. Within this assignment, the set of Raman frequencies was analyzed using the deduced diameters and the relation

$$\bar{\nu}_{\text{RBM}} = \frac{A}{d_t} + B$$

to find optimal values for parameters A and B (13). We repeated this process of Raman frequency analysis for each candidate assignment. Figure 3A shows the resulting root mean square (rms) error in fitting the Raman frequencies as a function of parameter A (with B optimized) for the leading candidates. Assignment “a” is strongly preferred because of its sharp minimum and low error of only 1 cm^{-1} . In addition, the deduced RBM parameters of $A = 223.5 \text{ cm}^{-1} \text{ nm}$ and $B = 12.5 \text{ cm}^{-1}$ for assignment “a” agree satisfactorily with prior independent reports (14–18). Figure 3B is a plot of measured RBM Raman frequencies versus inverse nanotube diameter in the chosen assignment “a,” along with a

line computed from the optimized parameters. Table 1 lists the set of observed transition wavelengths, corresponding photon energies, deduced (n,m) assignments, and RBM frequencies. Figure 4A shows, on a graphene lattice, the 33 nanotube structures identified through spectroscopic analysis of our sample.

The deduced assignment implies a match within 10% in the numbers of observed fluorescing nanotube species with $\text{mod } 3 = 1$ and $\text{mod } 3 = 2$. With spectral features assigned to specific (n,m) species, the relative abundances of those species may be determined from the intensities of the corresponding features. Figure 4B shows the measured fluorescence intensity as a function of nanotube diameter and chiral angle. Lacking specific knowledge of any variations of nanotube

fluorescence quantum yields with diameter or chiral angle, we presume that the distribution shown as a smoothed surface in Fig. 4B closely reflects the distribution of nanotube abundance in the sample. The measured distribution has a peak in diameter near 0.93 nm and extends from approximately 0.6 to 1.3 nm at $\sim 2\%$ of the peak value. In the chiral angle dimension, intensity falls from a maximum at the largest angles (near-armchair) to a minimum at 0° (zigzag), with no zigzag species detected in our data. It has been suggested that armchair chiralities may be favored by greater stability of armchair-like edge structures during the HiPco growth process (19). In contrast to prior electron nanodiffraction measurements on SWNT bundles, which have deduced both arm-

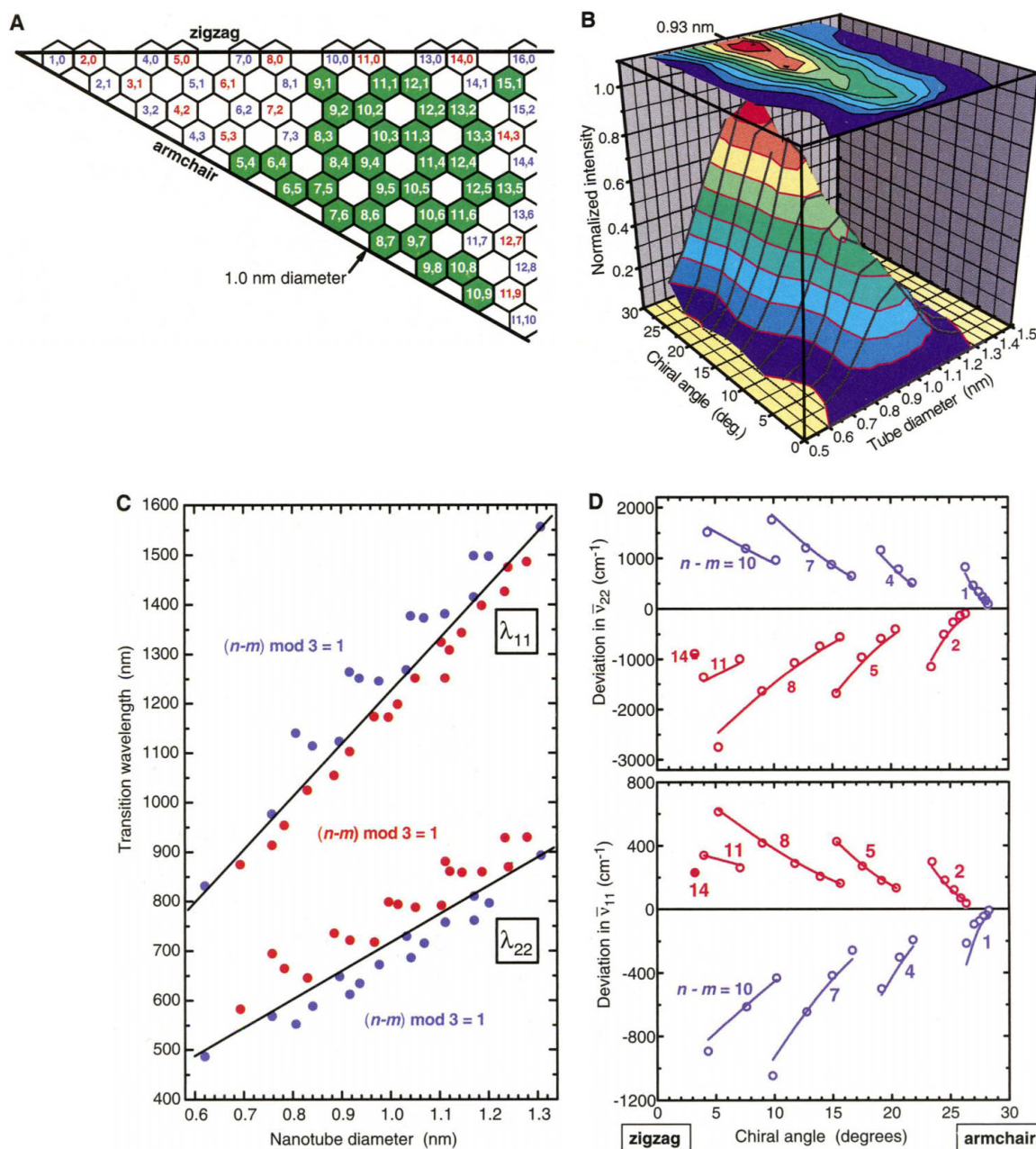
chair-rich and uniform chirality abundances (20, 21), our spectroscopic approach reveals distributions for isolated nanotubes contained in bulk samples.

Variations of transition energies with diameter and chirality are also of substantial interest for understanding nanotube electronic states and excitations. The simplest theoretical treatments predict that the optical transition wavelengths of semiconducting nanotubes depend linearly on diameter according to the relations

$$\lambda_{11} = \frac{hcd_t}{2a_{cc}\gamma_0} \quad \text{and} \quad \lambda_{22} = \frac{hcd_t}{4a_{cc}\gamma_0}$$

where d_t is the tube diameter, a_{cc} is the C-C bond distance, and γ_0 is the interaction energy between neighboring C atoms (22). In Fig. 4C,

Fig. 4. Results from the deduced spectral assignment. **(A)** Observed nanotube structures marked as green hexagons with white (n,m) labels on a graphene lattice. Other structures have blue or red labels for $(n-m) \bmod 3 = 1$ or 2, respectively. **(B)** Smoothed surface plot of fluorescence intensity as a function of nanotube diameter and chiral angle. **(C)** Measured optical transition wavelengths λ_{11} and λ_{22} versus nanotube diameter. Again, blue and red symbols code for values of $(n-m) \bmod 3$. **(D)** Frequency differences between data points and straight lines in (B) plotted versus chiral angle of the nanotube structure. Circles are experimental points; lines show values from the simple model fit described in the text.



we plot measured optical transition wavelengths λ_{11} and λ_{22} versus deduced tube diameter. Deviations from linear relations are obvious and in qualitative agreement with the pattern expected from trigonal warping effects in carbon nanotubes (6, 7). Such effects shift transition frequencies from the linear relation in a direction that depends on the value of $(n - m) \bmod 3$ and that reverses between first and second van Hove branches. Figure 4C also shows straight lines representing our best estimates of the undeviated transition wavelengths as a function of tube diameter. These lines separate the sets of transitions observed for $\bmod 3 = 1$ and $\bmod 3 = 2$ species.

To analyze spectral deviations in more detail, we computed frequency differences between the observed transitions and those indicated for the same tube diameter by the lines in Fig. 4C. These deviations, shown as open circles, are plotted as a function of nanotube chiral angle (α) in Fig. 4D. Also shown are solid lines with values computed from a simple model in which deviations are given by $A_i \cos(3\alpha)/d_t^2$. We selected this functional dependence on chiral angle and diam-

eter from theories of trigonal warping effects (6, 7), and we allowed the A_i factors to vary with the value of $(n - m) \bmod 3$ and with the van Hove transition index, i , to optimize agreement with the experiment. Although there are some systematic differences between this model and the data in Fig. 4D, the qualitative agreement is excellent. In addition, the results show clear patterns within and between families, which are labeled in the figure with their $n - m$ values.

By combining empirical expressions for the linear "undeviated" wavelengths with those for the deviations, we obtain the following formulas for first and second van Hove optical transition frequencies of SWNTs as a function of their diameter (in nm) and chiral angle

$$\bar{\nu}_{11} = \frac{1 \times 10^7 \text{ cm}^{-1}}{157.5 + 1066.9 d_t} + \frac{A_1 \cos(3\alpha)}{d_t^2}$$

with $A_1 = -710 \text{ cm}^{-1}$ for $(n - m) \bmod 3 = 1$ or $A_1 = 369 \text{ cm}^{-1}$ for $(n - m) \bmod 3 = 2$; and

$$\bar{\nu}_{22} = \frac{1 \times 10^7 \text{ cm}^{-1}}{145.6 + 575.7 d_t} + \frac{A_1 \cos(3\alpha)}{d_t^2}$$

with $A_2 = 1375 \text{ cm}^{-1}$ for $(n - m) \bmod 3 = 1$ or $A_2 = -1475 \text{ cm}^{-1}$ for $(n - m) \bmod 3 = 2$. These simple formulas will be valuable for predicting transitions of nanotube species not observed in our samples, including larger diameter tubes produced by other growth processes. Using four adjusted parameters for each branch, the formulas describe observed transitions with average errors of less than 65 cm^{-1} (8 meV) for $\bar{\nu}_{22}$ and 35 cm^{-1} (4 meV) for $\bar{\nu}_{11}$. These values fall well within the spectral line widths found for these transitions, which are approximately 400 to 800 cm^{-1} (50 to 100 meV) for $\bar{\nu}_{22}$ and 200 cm^{-1} (25 meV) for $\bar{\nu}_{11}$.

Our results provide a simple and practical spectroscopic route for finding the detailed composition of bulk nanotube samples. This method can be adapted for rapid analysis to guide processes that produce or sort nanotubes selectively by structure. In the area of nanotube physics, we find that optical transition frequencies deviate from a simple diameter dependence more strongly than expected. For example, the $\bar{\nu}_{22}$ value of the (9,2) tube is 26% higher (by 3700 cm^{-1} or 0.46 eV) than that of (9,1), even though its diameter is 6% larger. In addition, as tube diameter increases, the $\bar{\nu}_{22}/\bar{\nu}_{11}$ ratio apparently approaches a value smaller than 2 (23), which is predicted by most theories (6). It seems likely that phenomena beyond simple trigonal warping, and possibly including strong exciton effects (24, 25), will be revealed by quantitative theoretical analysis of these nanotube spectral data.

Table 1. Spectral data and assignments for SWNTs.

λ_{11} (nm)	λ_{22} (nm)	$h\nu_{11}$ (eV)	$h\nu_{22}$ (eV)	Assignment	Predicted $\bar{\nu}_{\text{RBM}}$ (cm^{-1})*	Observed $\bar{\nu}_{\text{RBM}}$ (cm^{-1})
833	483	1.488	2.567	(5,4)	372.7	373†
873	581	1.420	2.134	(6,4)	335.2	
912	693	1.359	1.789	(9,1)	307.4	
952	663	1.302	1.870	(8,3)	298.1	297‡
975	567	1.272	2.187	(6,5)	307.4	
1023	644	1.212	1.925	(7,5)	281.9	283‡
1053	734	1.177	1.689	(10,2)	265.1	264§
1101	720	1.126	1.722	(9,4)	256.4	
1113	587	1.114	2.112	(8,4)	278.3	
1122	647	1.105	1.916	(7,6)	262.1	264‡
1139	551	1.088	2.250	(9,2)	289.7	
1171	797	1.059	1.556	(12,1)	237.0	236
1172	716	1.058	1.732	(8,6)	243.7	
1197	792	1.036	1.565	(11,3)	232.8	233¶
1244	671	0.997	1.848	(9,5)	241.4	
1250	633	0.992	1.959	(10,3)	251.1	251‡
1250	786	0.992	1.577	(10,5)	225.1	225¶
1263	611	0.982	2.029	(11,1)	256.4	
1267	728	0.979	1.703	(8,7)	228.9	
1307	859	0.949	1.443	(13,2)	211.9	
1323	790	0.937	1.569	(9,7)	214.9	215¶
1342	857	0.924	1.447	(12,4)	207.5	
1372	714	0.904	1.736	(11,4)	221.5	
1376	685	0.901	1.810	(12,2)	227.0	
1380	756	0.898	1.640	(10,6)	213.4	
1397	858	0.887	1.445	(11,6)	200.8	
1414	809	0.877	1.533	(9,8)	203.4	
1425	927	0.870	1.337	(15,1)	193.6	
1474	868	0.841	1.428	(10,8)	192.5	
1485	928	0.835	1.336	(13,5)	187.2	
1496	795	0.829	1.559	(12,5)	198.3	
1497	760	0.828	1.631	(13,3)	203.4	
1555	892	0.797	1.390	(10,9)	183.3	

*Using the expression $\bar{\nu}_{\text{RBM}} = \frac{223.5}{d_t} + 12.5$ and assuming a C-C bond distance of 0.144 nm. †Raman

excitation wavelength 830 nm. ‡Raman excitation wavelengths 633 nm and 636 to 672 nm. §Raman excitation wavelength 1064 nm. ||Raman excitation wavelength 782 nm. ¶Raman excitation wavelength 785 nm.

References and Notes

1. M. S. Dresselhaus, G. Dresselhaus, P. C. Klund, *Science of Fullerenes and Carbon Nanotubes* (Academic Press, San Diego, CA, 1996).
2. M. O'Connell et al., *Science* **297**, 593 (2002).
3. T. W. Odum, J.-L. Huang, P. Kim, C. M. Lieber, *J. Phys. Chem. B* **104**, 2794 (2000).
4. H. Kataura et al., *Synth. Met.* **103**, 2555 (1999).
5. S. Reich, J. Maultzsch, C. Thomsen, P. Ordejon, *Phys. Rev. B* **66**, 035412 (2002).
6. R. Saito, G. Dresselhaus, M. S. Dresselhaus, *Phys. Rev. B* **61**, 2981 (2000).
7. S. Reich, C. Thomsen, *Phys. Rev. B* **62**, 4273 (2000).
8. Examples of adjacent points on linking curves would be (10,5) and (11,3), or (10,5) and (8,6). The linking curve pattern is most easily seen from Fig. 1A. When the pattern crosses the armchair line to denote structures with $m > n$, the n and m indices should be interchanged.
9. A. M. Rao et al., *Science* **275**, 187 (1997).
10. M. S. Dresselhaus, G. Dresselhaus, A. Jorio, A. G. Souza Filho, R. Saito, *Carbon* **40**, 2043 (2002).
11. S. Bandow et al., *Phys. Rev. Lett.* **80**, 3779 (1998).
12. G. S. Duesberg et al., *Chem. Phys. Lett.* **310**, 8 (1999).
13. The Raman offset term, B , has generally been associated with bundling effects in nanotube spectra. We include it here only to obtain a better empirical fit to data. Assignment "a" remains preferred when B is forced to zero.
14. J.-L. Sauvajol, E. Anglaret, S. Rols, L. Alvarez, *Carbon* **40**, 1697 (2002).
15. G. Sauve, P. V. Kamat, R. S. Ruoff, *J. Phys. Chem.* **99**, 2162 (1995).
16. Z. Yu, L. Brus, *J. Phys. Chem. B* **105**, 6831 (2001).
17. U. D. Venkateswaran et al., *Phys. Rev. B* **59**, 10928 (1999).
18. L. Alvarez et al., *Chem. Phys. Lett.* **316**, 186 (2000).

19. A. Thess *et al.*, *Science* **273**, 483 (1996).
 20. J. M. Cowley, P. Nikolaev, A. Thess, R. E. Smalley, *Chem. Phys. Lett.* **265**, 379 (1997).
 21. L.-C. Qin, S. Iijima, *Chem. Phys. Lett.* **269**, 65 (1997).
 22. R. Saito, G. Dresselhaus, M. S. Dresselhaus, *Physical Properties of Carbon Nanotubes* (Imperial College Press, London, 1998).
 23. The chiral angle approaches 30° for each family of nanotube structures in the limit of long transition wavelengths (large diameters).
 24. T. Ando, *J. Phys. Soc. Jpn.* **66**, 1066 (2001).
 25. M. Ichida, S. Mizuno, Y. Tani, Y. Saito, A. Nakamura, *J. Phys. Soc. Jpn.* **68**, 3131 (1999).
 26. Supported by NSF (grant CHE-9900417), the NSF Focused Research Group on Fullerene Nanotube Chemistry (grant DMR-0073046), the NSF Center for Biological and Environmental Nanotechnology (grant EEC-0118007), and the Robert A. Welch Foundation (grants C-0807 and C-0689). Support from NASA (grant NCC 9-77) for development of the HiPco method is also gratefully acknowledged. We thank M. O'Connell and V. Moore for assistance in sample

preparation, S. Doorn for Raman spectroscopy, the University of Illinois Materials Research Laboratory for use of facilities, S. Reich for generously sharing computer codes and extended tight binding results before publication, and G. Mele for helpful and stimulating discussions.

24 September 2002; accepted 11 November 2002
 Published online 28 November 2002;
 10.1126/science.1078727
 Include this information when citing this paper.

Microporous and Photoluminescent Chalcogenide Zeolite Analogs

Nanfeng Zheng,¹ Xianhui Bu,² Bing Wang,¹ Pingyun Feng^{1*}

Crystalline semiconducting sulfide and selenide zeolite analogs were synthesized that possess four-connected, three-dimensional tetrahedral networks built from tetravalent ($M^{4+} = Ge^{4+}$ or Sn^{4+} , where M = meta) and trivalent ($M^{3+} = Ga^{3+}$ or In^{3+}) cations. Microporous materials were obtained in all four combinations of M^{4+} and M^{3+} , and some of them were thermally stable up to at least 380°C. These materials exhibit framework topologies with pore size ranging from 12 to 24 tetrahedral atoms, high surface area, high framework charge density and ion exchange capacity, and tunable electronic and optical properties.

Microporous materials exemplified by aluminosilicate zeolites have large-scale commercial applications ranging from gas separation

to petroleum processing (1). For ~50 years, there has been interest in developing porous materials with either novel chemical compositions or new framework topologies because properties and applications of porous materials are intimately related to their compositional and topological features (2, 3). In general, the synthesis of new porous materials involves the replacement of tetrahedral atoms

(T atoms), such as Al^{3+} or Si^{4+} , in zeolites by other T atoms, such as Ga^{3+} , Ge^{4+} , and P^{5+} (4). Resulting oxides are usually insulators and have very limited electro-optic applications.

To expand microporous materials beyond their traditional applications, researchers have found that it is desirable to synthesize microporous semiconducting materials. Crystalline porous semiconductors may find applications in electrocatalysis, photocatalysis, and electrochemical sensor analysis, where size and shape of chemical and biochemical agents are important for selectivity. Analytical applications have the potential for exceptionally high sensitivity because of the pre-concentration effect of porous materials through adsorption or ion exchange.

One of the most important goals in developing crystalline porous semiconductors is to generate three-dimensional (3D) frameworks with enhanced thermal stability. Since the late 1980s, research involving porous chalcogenides has received increasing attention with the synthesis of a number of open-framework chalcogenides (5–10). When only tetravalent metal cations, such as Ge^{4+} or Sn^{4+} , are used to build chalcogenide frame-

¹Department of Chemistry, University of California, Riverside, CA 92521, USA. ²Department of Chemistry, University of California, Santa Barbara, CA 93106, USA.

*To whom correspondence should be addressed. E-mail: pingyun.feng@ucr.edu

Table 1. A summary of crystallographic data for selected UCR-20, UCR-21, UCR-22, and UCR-23 structures. Crystal structures were solved from single-crystal data collected at 298 K on a SMART 1000 charge-coupled device diffractometer with Mo K α . For UCR-21InSnS-AEP, $b = 16.943 \pm 0.003$ Å. Standard deviations for a and c are given by the numbers in parentheses, with the number representing the deviation in the least

significant digit(s). TAEA = tris(2-aminoethyl)amine, $C_6H_{18}N_4$; TMDP = 4,4'-trimethylenedipiperidine, $C_{13}H_{26}N_2$; APO = *dl*-1-amino-2-propanol, C_3H_9NO ; APP = 1-(3-aminopropyl)-2-pipecoline, $C_9N_2H_{20}$; AEP = 1-(2-aminoethyl)piperazine, $C_6H_{15}N_3$; TOTDA = 4,7,10-trioxa-1,13-tridecanediamine, $C_{10}H_{24}N_2O_3$; AEM = *N*-(2-aminoethyl)morpholine, $C_6H_{14}N_2O$. $R(F) = \sum |F_{obs}| - |F_{calc}| / \sum |F_{obs}|$ with $F_{obs} > 4.0\sigma(F)$.

Structure	Framework composition	Space group	a (Å)	c (Å)	$R(F)$
UCR-20GaGeS-TAEA	$Ga_{2.67}Ge_{1.33}S_8$	$-4 \rightarrow \bar{4}$	20.9352(15)	20.9352(15)	7.21
UCR-20GaSnS-TMDP	$Ga_{1.80}Sn_{2.20}S_8$	$-4 \rightarrow \bar{4}$	21.5404(17)	21.5404(17)	5.54
UCR-20InGeS-TMDP	$In_{3.00}Ge_{1.00}S_8$	$-4 \rightarrow \bar{4}$	21.734(2)	21.734(2)	7.61
UCR-20InSnS-TMDP	$In_{2.50}Sn_{1.50}S_8$	$-4 \rightarrow \bar{4}$	22.1906(18)	22.1906(18)	7.61
UCR-20GaGeSe-TMDP	$Ga_4Ge_4Se_8$	$-4 \rightarrow \bar{4}$	21.893(2)	21.893(2)	7.40
UCR-21GaGeS-APO	$Ga_{3.30}Ge_{0.70}S_8$	$-4 \rightarrow \bar{4}$	11.1414(15)	19.405(4)	4.18
UCR-21GaSnS-TAEA	$Ga_{2.32}Sn_{1.68}S_8$	$-4 \rightarrow \bar{4}$	11.6915(19)	19.898(5)	4.46
UCR-21InGeS-APP	$In_{1.84}Ge_{2.16}S_8$	$-4 \rightarrow \bar{4}$	11.5313(15)	19.936(4)	6.94
UCR-21InSnS-AEP	$In_xSn_{4-x}S_8$	$-4 \rightarrow \bar{4}$	13.379(2)	25.973(5)	6.48
UCR-21GaSnSe-TAEA	$Ga_{2.47}Sn_{1.53}Se_8$	$-4 \rightarrow \bar{4}$	12.5373(19)	20.564(4)	6.04
UCR-22GaGeS-AEP	$Ga_{3.33}Ge_{0.67}S_8$	$-4 \rightarrow \bar{4}$	22.532(2)	39.954(5)	6.23
UCR-22GaSnS-AEP	$Ga_{2.13}Sn_{1.87}S_8$	$-4 \rightarrow \bar{4}$	22.935(2)	40.985(6)	5.51
UCR-22InGeS-AEP	$In_{2.69}Ge_{1.31}S_8$	$-4 \rightarrow \bar{4}$	22.9078(12)	41.490(3)	5.82
UCR-22GaSnSe-TOTDA	$Ga_{1.73}Sn_{2.27}S_8$	$-4 \rightarrow \bar{4}$	23.841(3)	42.555(7)	6.83
UCR-23GaGeS-AEM	$Ga_{2.67}Ge_{1.33}S_8$	$-4 \rightarrow \bar{4}$	21.638(3)	11.209(2)	5.43
UCR-23GaSnS-AEM	$Ga_{2.29}Sn_{1.71}S_8$	$-4 \rightarrow \bar{4}$	22.169(3)	11.3168(18)	5.68
UCR-23InGeS-AEM	$In_{1.84}Ge_{2.16}S_8$	$-4 \rightarrow \bar{4}$	22.153(3)	11.3435(18)	6.79